

Hyperbolic plasmon modes in tilted Dirac cone phases of borophene

Zahra Torbatian,¹ Dino Novko,^{2,3,*} and Reza Asgari^{4,5,6,†}

¹ School of Nano Science, Institute for Research in Fundamental Sciences (IPM), Tehran 19395-5531, Iran

² Institute of Physics, Bijenička 46, 10000 Zagreb, Croatia

³ Donostia International Physics Center (DIPC), Paseo Manuel de Lardizabal 4, 20018 Donostia-San Sebastián, Spain

⁴ School of Physics, Institute for Research in Fundamental Sciences (IPM), Tehran 19395-5531, Iran

⁵ School of Physics, University of New South Wales, Kensington, NSW 2052, Australia

⁶ ARC Centre of Excellence in Future Low-Energy Electronics Technologies, UNSW Node, Sydney 2052, Australia

Hyperbolic materials are receiving significant attention due to their ability to support electromagnetic fields with arbitrarily high momenta and, hence, to achieve very strong light confinement. Here, based on first-principles calculations and many-body perturbation theory, we explore the characteristic of two-dimensional plasmon modes and its hyperbolic properties for two phases of single layer boron hosting tilted Dirac cone, namely, the *hr-sB* and *8Pmmn* borophene. In-plane anisotropy in borophene is manifested in the structural, electronic, vibrational and optical properties. We find two hyperbolic regimes for both phases of borophene, where the high-energy one is located in the visible range. The *hr-sB* borophene is characterised with an intrinsic high carrier density and it supports strong hyperbolic plasmon modes in the visible part of the spectrum. The *8Pmmn* borophene, on the other hand, resembles the prototypical Dirac material graphene, and upon carrier doping acquires anisotropic Dirac plasmons in the mid-infrared. We have also investigated the impact of the electron-phonon coupling and Landau damping on these hyperbolic plasmon modes. Our results show that borophene, having high anisotropy, intrinsic high carrier concentration, low-loss hyperbolic Dirac plasmon modes, and high confinement can represent a promising candidate for low-loss broad band surface plasmon polariton devices.

INTRODUCTION

Natural hyperbolic materials with anisotropic dielectric constants where the real parts of the principle components have opposite signs, have recently attracted many attention [1–6]. These materials support electromagnetic modes with large wave-vector and exhibit directionally propagating polaritons with extremely large photonic density of states [2, 7–9]. Polaritons in natural materials can be formed when the light interacts with the intrinsic plasmons, phonons, or excitons [10, 11]. In contrast to the artificial metasurfaces, where hyperbolic dispersion is limited to wave-vectors smaller than the inverse of the structure size, natural hyperbolic materials support high electromagnetic confinement and contain no internal interfaces for the electrons to scatter off [2]. Naturally occurring hyperbolic plasmonic media are rare and thus far they were experimentally verified to exist only in the WTe₂ thin film [12, 13]. However, recent theoretical studies have predicted interesting hyperbolic properties not only in WTe₂ [14], but as well in black phosphorus [8, 15, 16], cuprates, MgB₂ [2], electrides [17], MoTe₂ [18, 19], layered hexagonal crystal structures [20] and MoOCl₂ [21]. Generally, ideal natural hyperbolic plasmonic material is needed to possess high structural and electronic anisotropy, high carrier density and low plasmonic losses. Here, we propose two phases of borophene with such electronic and optical properties that might be naturally suitable to serve as an efficient

hyperbolic plasmonic material.

Recently two-dimensional (2D) boron with high free charge carrier concentration emerged as a perfect 2D metal with extraordinary electric, optical and transport properties [22–31]. In fact, borophene, as an intrinsic 2D metal with both high carrier density and high confinement, can be a promising candidate to develop optical devices based on low-loss broad band surface plasmon polaritons [29, 32]. Until now, a number of monolayer boron sheets have been theoretically predicted and three types of borophene fabricated in the experiment, i.e., strip, β_{12} , and χ_3 borophene [33, 34].

In this paper, we investigate two phases of borophene, namely, *8Pmmn* and *hr-sB*. The first one represent a polymorph of borophene which hosts an anisotropic tilted Dirac cone [35–37]. The Dirac cone was thus far confirmed to exist in the β_{12} phase of borophene on Ag(111) [38] and indicated in reconstructed borophene polymorph on Ir(111) [39]. The second one, i.e., *hr-sB*, is a newly predicted boron monolayer with two types of Dirac fermions coexisting in the sheet; one type is related to Dirac nodal lines and the other is related to tilted semi-Dirac cones with strong anisotropy. This new allotrope possesses a high stability compared to the experimentally available δ_6 , β_{12} and χ_3 sheets [40]. Here, we investigate characteristics of 2D Dirac plasmons and its hyperbolic properties for these two phases of borophene in the framework of density functional theory and many-body perturbation theories. Our results show that both phases of borophene support strong Dirac hyperbolic plasmons due to their highly anisotropic optical properties. Owing to the high intrinsic carrier concentration, hyperbolic Dirac plasmons in the *hr-sB* borophene are present also

* dino.novko@gmail.com

† asgari@ipm.ir

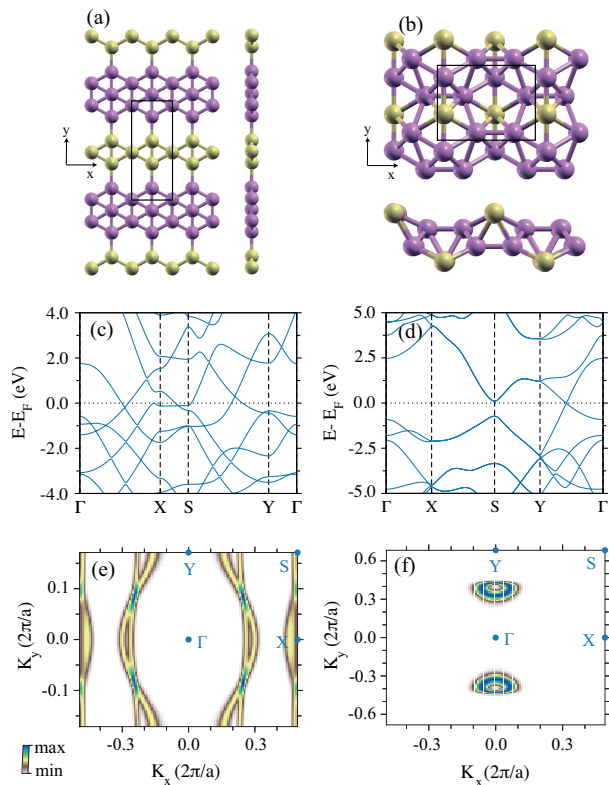


FIG. 1. **Geometric and electronic structure of borophene.** Top and side views of optimized (a) *hr-sB* and (b) *8Pmmn* borophene structures. The electronic band structure along high symmetry direction of *hr-sB* and *8Pmmn* are shown in (c) and (d), respectively. Panels (e) and (f) show the Fermi surfaces of pristine *hr-sB* and hole doped *8Pmmn* ($E_F = -250$ meV). The boron atoms in the hexagon stripes (B_h) (inner atoms B_I) and in rhombus stripse (B_r) (ridge atoms B_R) are indicated in purple and yellow, respectively, in the *hr-sB* (*8Pmmn*) phase. The primitive unit cell in both structures is marked by the black rectangle.

in the visible range. In addition, we explore the coupling of Dirac plasmons with phonons as well as with the electron-hole pairs from first principles. This allows us to study the decay rates of plasmons in borophene and asses its efficiency both qualitatively and quantitatively. Interestingly, we find extremely negligible plasmonic losses in the *8Pmmn* borophene, which are actually comparable to the losses in prototypical Dirac material graphene. Therefore, these novel 2D hyperbolic Dirac materials are promising and appealing for applications in plasmonics.

RESULTS AND DISCUSSION

Electronic structure of borophene.— In Fig. 1 we display the optimized structure and electronic bands along high-symmetry points for the *hr-sB* and *8-Pmmn* phases of borophene. The unit cells of both phases are

rectangular and contain eight atoms. In contrast to the *8Pmmn* phase with buckled structure, the *hr-sB* phase is purely planar with stripes of hexagons and rhombs along the x axis [see Fig. 1(a)]. The boron atoms are called B_h and B_r in the hexagon and rhomb stripes, respectively. The *8Pmmn* borophene structure contains two types of non-equivalent B atoms, namely the ridge atoms (B_R) and the inner atoms (B_I) [see Fig. 1(b)], leading to various physical and chemical properties. Figure 1(c) shows the anisotropic band structure of *hr-sB* with a Dirac nodal line and tilted semi-Dirac cones coexisting around the Fermi energy [38]. Two linear bands are crossed between Γ and X points as well as between S and Y points forming Dirac point slightly below and above the Fermi level. Actually, these apparently two structures are part of the Dirac nodal line, which can be seen from the Fermi surface plot in Fig. 1(e). The tilted Dirac cone is at the edge of the Brillouin zone (BZ). The orthorhombic *8Pmmn* borophene possesses tilted anisotropic Dirac cone along the ΓY path, where the Dirac point crosses the Fermi level [see Fig. 1(d) and the corresponding Fermi surface with $E_F = -250$ meV in Fig. 1(f)]. It is worth mentioning that the Dirac cone of the *8Pmmn* borophene emerges from the symmetry of the hexagonal and topologically equivalent lattice to uniaxially strained graphene lattice [35].

In contrast to graphene where the two crossing linear bands both come from the p_z orbitals, in 2D boron allotropes the p_z orbitals are not the only dominating contribution to the Dirac cone. In the *hr-sB* sheet, the two crossing bands between the Γ and X points come from different orbitals originating in various atomic sites, i.e., the p_z orbitals of B_h atoms and the $p_{x/y}$ orbitals of B_r atoms have dominating contributions. Along the XS direction, p_z orbitals of both B_r and B_h atoms are contributing to the Dirac bands. Furthermore, the Dirac cones in *8Pmmn* are arising from the p_z orbitals of the B_I atoms with a much lesser contribution of the p_x orbitals. In this phase the B_R atoms do not contribute to the formation of the electronic states in the vicinity of the Fermi level, which is in line with the previous theoretical work [40].

The study of the EPC represents a fundamental and fascinating issue and it is the first step towards the calculations of the plasmon decay rates in the two phases of borophene. The dynamical matrices and phonon-perturbed potentials are calculated on a Γ -centered grid within the framework of density functional perturbation theory. In Figs. 2(a) and 2(b), we show the phonon dispersions and momentum-resolved $\lambda_{\mathbf{q},\nu}$ along the high symmetry points (superimposed as a color code to the corresponding dispersions), and phonon density of states (DOS) for two chosen phases of borophene. Note that for the *8Pmmn* borophene, the hole-doped case with $E_F = -250$ meV is considered. No imaginary vibrating mode is seen for the *hr-sB* phase of borophene, indicating the stability of this structure. In *8Pmmn* all the phonon modes are positive frequencies, except the transverse branch near the Γ point. Moreover, the re-

sults show the EPC strength is remarkable along the XS direction and near the Γ point for *hr-sB*. While the EPC strength in *8Pmmn* is weak and appears for the modes at the Γ and Y points. The prominent peaks in the phonon DOS of *hr-sB* structure are located around 50, 90, and 150 meV and are due to the dispersionless nature of the phonon band structure around these energies. In the *8Pmmn* phase the dispersionless phonon structures are also behind the peaks in the phonon DOS.

The Eliashberg function, $\alpha^2 F(\omega)$, the phonon-induced decay rate $1/\tau_{\text{ph}}(\omega)$ and energy renormalization parameter $\omega\lambda_{\text{ph}}(\omega)$ for the two phases of borophene are illustrated in Figs. 2(c)-(f). The feature of the Eliashberg function for the *hr-sB* structure does not follow the phonon DOS for energies below 50 meV but it resembles the phonon DOS above 50 meV. The most intense peaks come from the optical phonons near the Γ point and along the XS path, where momentum-resolved $\lambda_{\mathbf{q},\nu}$ appears to be the strongest [see Fig. 2(a)]. Similarly, the characteristic of the Eliashberg function for *8Pmmn* are completely unconnected to its phonon DOS and but mainly to its EPC strengths $\lambda_{\mathbf{q},\nu}$ [Fig. 2(b)]. Regarding the total EPC strength, we have obtained the values of $\lambda = 0.25$ and $\lambda = 0.008$ for *hr-sB* and *8Pmmn* phases of borophene, respectively. It is surprising that the EPC in *8Pmmn* is extremely small and it is therefore expected that the corresponding phonon-induced plasmon decay is also quite small.

Optical conductivity and hyperbolic regions.— We now turn to the study of anisotropic optical properties in borophene. The appearance of hyperbolic regions for certain photon energy can be inspected by calculating the optical conductivity for different light polarization directions. The corresponding hyperbolic condition for specific photon energy $\hbar\omega$ is defined as

$$\text{Im}[\sigma_x(\omega)] \times \text{Im}[\sigma_y(\omega)] < 0. \quad (1)$$

We display the imaginary (top) and the real (bottom) parts of optical conductivity along two principal axes for *hr-sB* (left) and *8Pmmn* (right) phases of borophene in Fig. 3. The hyperbolic regimes are depicted with the shaded area. The imaginary part of optical conductivity along the y axis for the *hr-sB* phase changes its sign around 1.0 eV and stays negative up to 1.58 eV. This demonstrates the first hyperbolic region in the *hr-sB* borophene. Interestingly, the second hyperbolic regime falls between 1.84 and 2.21 eV, i.e., in the visible range. The hyperbolicity condition for the *8Pmmn* phase of borophene is also met in the visible part of the spectrum, i.e., there is one small hyperbolic region around 1.66 eV, and one with the energy window going from 1.85 to 2.39 eV. In addition, the *8Pmmn* borophene displays hyperbolic behavior also at the lower energies between 0.085 and 0.27 eV (mid-infrared).

From the results of the real parts of the optical conductivity, indicating the allowed intraband and interband optical transitions, one can examine the origin of these hyperbolic regions. For instance, in both phases of

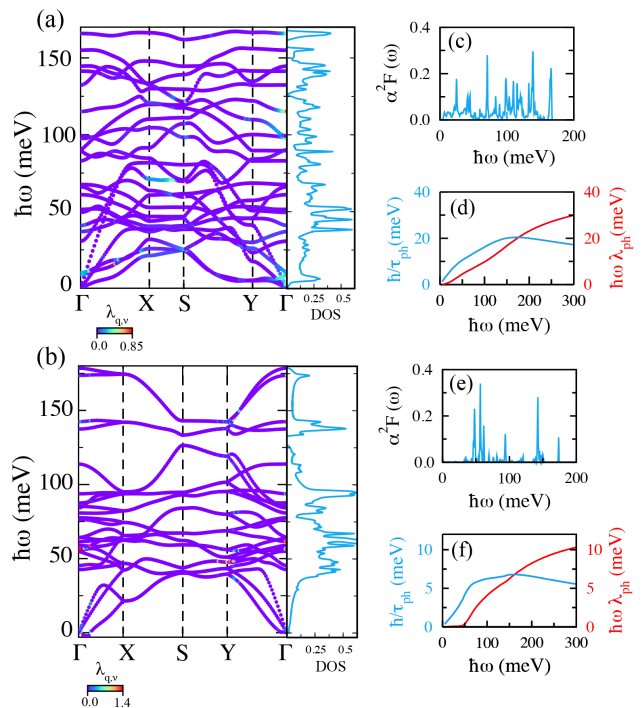


FIG. 2. **Vibrational properties and electron-phonon coupling in borophene.** The phonon band structure and momentum-resolved $\lambda_{\mathbf{q},\nu}$ along the high symmetry points together with the phonon density of states (DOS) for (a) pristine *hr-sB* and (b) hole-doped ($E_F = -250$ meV) *8Pmmn* phases of borophene. The Eliashberg function $\alpha^2 F(\omega)$, phonon-induced decay rate $1/\tau_{\text{ph}}(\omega)$, and energy renormalization parameter $\omega\lambda_{\text{ph}}(\omega)$ are shown in panels (c) and (d) for *hr-sB*, while for hole-doped *8Pmmn* in panels (e) and (f).

borophene, there are interband excitations between 1.5 and 2.5 eV, which are intense and allowed for the y direction, while forbidden and negligible for the x direction. In addition, the *8Pmmn* phase has strongly anisotropic intraband transitions (see the Drude peaks for the x and y directions below 0.2 eV). All these results suggest an extremely promising hyperbolic optical property of these two phases of borophene.

We further inspect the optical absorption of *hr-sB* that shows intense peaks due to interband transitions at energies below 3 eV, which can therefore interact with the Dirac plasmons. In Fig. 4 the real part of the interband optical conductivity $\text{Re}\sigma_{\mu}^{\text{inter}}(\omega)$ is shown for particular interband transitions for x and y polarizations, coming from three valence bands (VB-2, VB-1 and VB) below and three conduction bands (CB, CB+1 and CB+2) above the Fermi level. The most intense absorption peaks in the presented energy range stem from the interband transitions from VB to CB, from VB to CB+1, as well as from VB-1 to CB. We single out three interband excitations relevant for the Dirac plasmon: (i) the prominent interband peak at ~ 0.5 eV that is present for the GX direction, (ii) absorption peak at ~ 1.5 eV for the GY

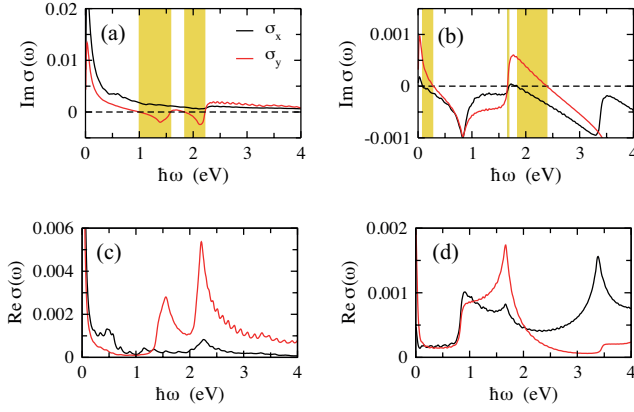


FIG. 3. **Polarization-dependent optical absorption and hyperbolic regions.** The imaginary (top panel) and real parts (bottom panel) of optical conductivity along the x (black line) and y (red line) directions for (a),(c) hr - sB and (b),(d) $8Pmmn$. The shaded areas show the hyperbolic regions in the both phases of borophene.

direction, and (iii) interband continuum that starts at ~ 1 eV for the ΓX direction. According to Fig. 4(b) the interband peak (i) comes entirely from the VB to CB transitions around the X point of the BZ. The feature (ii) originates from interband transitions around the Y point including VB-1, VB, CB, and CB+1. The continuum (iii) is due to interband transitions between VB-2 and CB as well as between VB-1 and CB both around the S point of the BZ.

Anisotropic dispersion and damping of Dirac plasmon.— In this section, we first study the plasmon dispersion of the hr - sB and $8Pmmn$ phases of borophene in the optical limit (small \mathbf{q}) for light polarization along the ΓX and ΓY directions, and with including the electron-phonon interaction. To do so, we adopt utilize the current-current (transverse) response formalism. We consider hr - sB phase in the pristine (undoped) form, however in the case of $8Pmmn$ the Fermi level is shifted 250 meV below the Dirac point to increase the carrier concentration. Figures 5(a) and 5(b) illustrate the plasmon dispersion of two phases of borophene along the two in-plane principal axes. The characteristics of the plasmon dispersion are seemed very much like in the typical 2D Dirac semimetal in the long-wavelength limit, showing $\sim \sqrt{q}$ dependence. However, there is a crucial difference here, namely the very pronounced anisotropy in plasmon dispersion along the ΓX and ΓY directions. This can be followed back to the strong anisotropy in the electronic structure [41] as well as to the anisotropy in the allowed optical (both intraband and interband) transitions along the two in-plane directions [as seen in Figs. 3(c) and 3(d)]. The similar behavior of 2D anisotropic plasmon dispersions has been reported in WTe_2 [14] and black phosphorous [8, 16, 42, 43]. It should be pointed out that such strong anisotropy could lead to hyperbolic plasmons

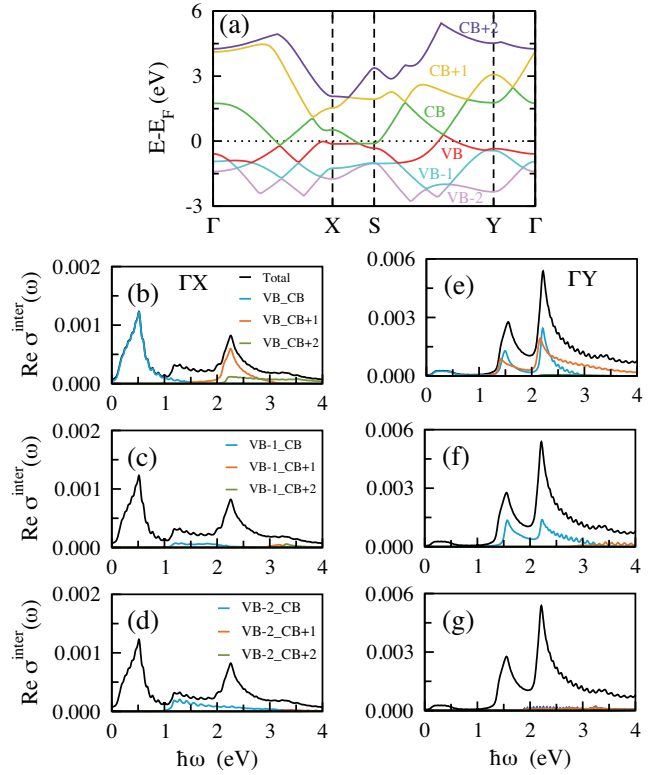


FIG. 4. **Interband contributions to optical absorption.** (a) The electronic band structure of hr - sB where three bands just below (VB-2, VB-1 and VB) and three bands just above the Fermi level (CB, CB+1 and CB+2) are illustrated with different colors. The different contributions to the interband optical absorption $\text{Re } \sigma_{\mu}^{\text{inter}}(\omega)$ of hr - sB coming from the transitions between the bands indicated in panel (a) when the polarization direction is along (b)-(d) ΓX and along (e)-(g) ΓY . Total optical absorption is shown with the black line.

in 2D materials [14]. Therefore, the combination of a high anisotropy and strong metallic character could make both phases of borophene promising 2D hyperbolic materials.

In the following, we discuss the temperature dependence of the plasmon linewidth due to the EPC. The case of hole-doped $8Pmmn$ borophene is additionally compared with the prototypical Dirac material graphene with $E_F = -250$ meV [44]. The damping rates \hbar/τ_{ph} as a function of the temperature for two phases of borophene and graphene when $\hbar\omega = 0.1$ eV and $\hbar\omega = 0.2$ eV are plotted in Figs. 6(a) and 6(b). Compared to the $8Pmmn$ borophene and graphene, the hr - sB phase of borophene shows the largest damping rate due to the EPC and steepest temperature increase. For the presented plasmon energies, plasmon in graphene has the lowest damping rate. This is because under these conditions (i.e., $T \leq 300$ K and $\hbar\omega \leq 0.2$ eV), graphene plasmon is only weakly coupled to acoustic phonons [44], while in both phases of borophene due to more complex structure there are multiple low-energy optical and acoustic phonons

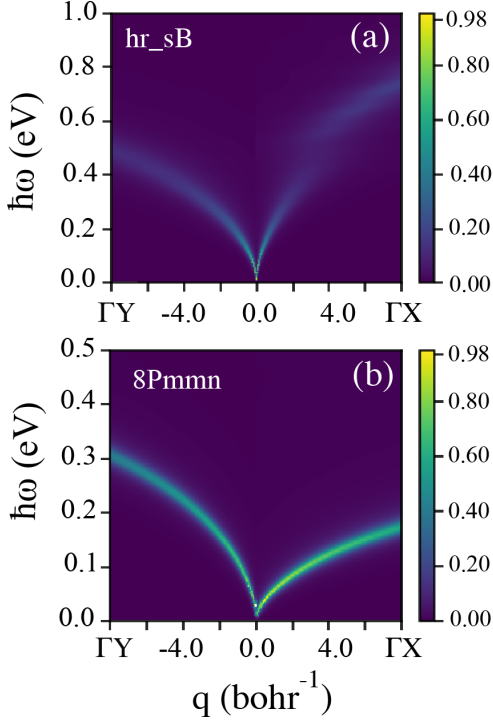


FIG. 5. **Hyperbolic Dirac plasmons in optical limit.** Plasmon dispersions as a function of q (in 10^{-3} bohr $^{-1}$) with incorporating the electron-phonon coupling at $T = 0$ K for (a) pristine *hr-sB* and (b) hole doped *8Pmmn* ($E_F = -250$ meV) phase of borophene along two principal axes, i.e., ΓX and ΓY directions.

that can couple to Dirac plasmon [see Fig. 2].

To perform a more thorough survey of plasmon damping, we calculate the total damping of plasmon that additionally includes Landau damping (coupling to electron-hole pair transitions) by making use of the following expression [45].

$$\hbar\Gamma(\mathbf{q}, \omega) = 2\pi\hbar q \text{Re}\{\sigma_\mu(\mathbf{q}, \omega)\} \quad (2)$$

where $\sigma_\mu(\mathbf{q}, \omega)$ contains both intraband $\sigma_\mu^{\text{intra}}(\mathbf{q}, \omega)$ and interband $\sigma_\mu^{\text{inter}}(\mathbf{q}, \omega)$ terms. The total damping for all three systems is illustrated in Figs. 6(c) and 6(d). For two phases of borophene, $\hbar\Gamma(\mathbf{q}_{\text{pl}}, \omega_{\text{pl}})$ is plotted along the ΓX and ΓY directions. As expected, the total damping in the *hr-sB* phase of borophene is considerably larger than in the *8Pmmn* phase and graphene, because both EPC and interband transitions are stronger in *hr-sB* [compare the intensities of $\text{Re}\sigma_\mu$ in Figs. 3(c) and 3(d)]. Interestingly, the total plasmon damping of *8Pmmn* and graphene are remarkably similar at $\hbar\omega_{\text{pl}} \leq 0.3$ eV. Furthermore, the total damping of Dirac plasmon in the *hr-sB* phase shows a specific sharp increase at ~ 0.5 eV, followed by a decrease, but only in the ΓX direction. This interesting feature (*i*) that is only allowed for the x polarization [compare $\text{Re}\sigma_x(\omega)$ and $\text{Re}\sigma_y(\omega)$ around 0.5 eV in Figs. 4(b)

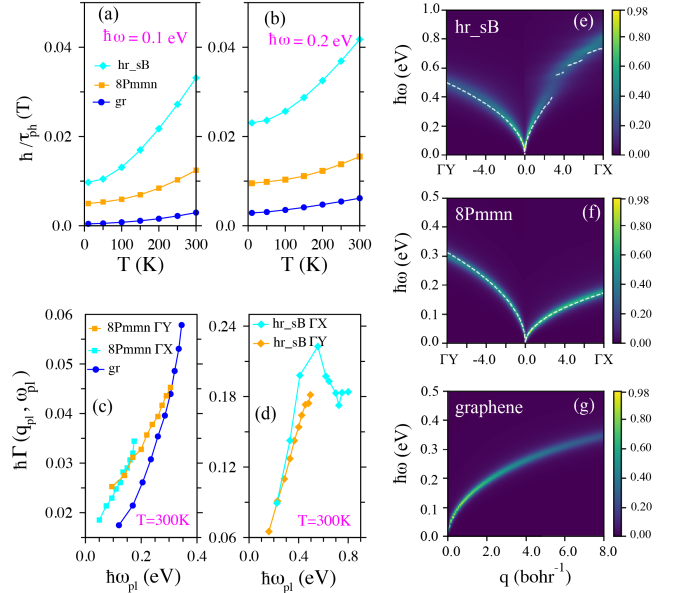


FIG. 6. **Coupling of hyperbolic Dirac plasmons and phonons.** Plasmon damping rates owing to the electron-phonon coupling $\hbar/\tau_{\text{ph}}(\omega)$ as a function of the temperature for *hr-sB*, *8Pmmn* and graphene when energy is (a) $\hbar\omega = 0.1$ eV and (b) $\hbar\omega = 0.2$ eV. Total damping of plasmon which additionally includes Landau damping along the x and y directions and $T = 300$ for (c) graphene and *8Pmmn* ($E_F = -250$ meV) as well as for (d) *hr-sB*. Plasmon dispersions of (e) *hr-sB*, (f) *8Pmmn*, and (g) graphene as a function of q (in 10^{-3} bohr $^{-1}$) when the electron-phonon coupling is included at $T = 300$ K. The white dashed lines in (e) and (f) show the plasmon dispersions at $T = 0$ K for *hr-sB* and *8Pmmn*, respectively.

and 4(e)]. Note that this coupling between Dirac plasmon and interband transitions (*i*) also results in avoided crossing in plasmon dispersion along the ΓX direction, as observed in Figs. 5(a) and 6(e).

Figures 6(e)-(g) show the plasmon dispersions of pristine *hr-sB* as well as hole-doped *8Pmmn* and graphene ($E_F = -250$ meV) along two principal axes at $T = 300$ K. The temperature dependence of the plasmon energy comes from the Fermi-Dirac distribution function and also from the EPC through $1/\tau_{\text{ph}}(\omega)$ and $\lambda_{\text{ph}}(\omega)$ functions. The temperature dependence of the plasmon dispersion due to the EPC is remarkable for the *hr-sB* borophene. On the other hand, the temperature dependence of the plasmon dispersion is weak in *8Pmmn* and graphene owing to the weak coupling of plasmon and phonons in these two materials. To have an insight into the temperature dependence of the plasmon, we illustrate the plasmon dispersions at $T = 0$ K for *hr-sB* and *8Pmmn* with the white dashed line in Figs. 6(e) and (f) respectively. For *8Pmmn*, it is obvious that the change in dispersion is negligible. On the other hand, it is considerable for *hr-sB*, especially along the ΓX where it changes from 0.73 eV to 0.80 eV at largest q vector (8×10^{-3} bohr $^{-1}$)

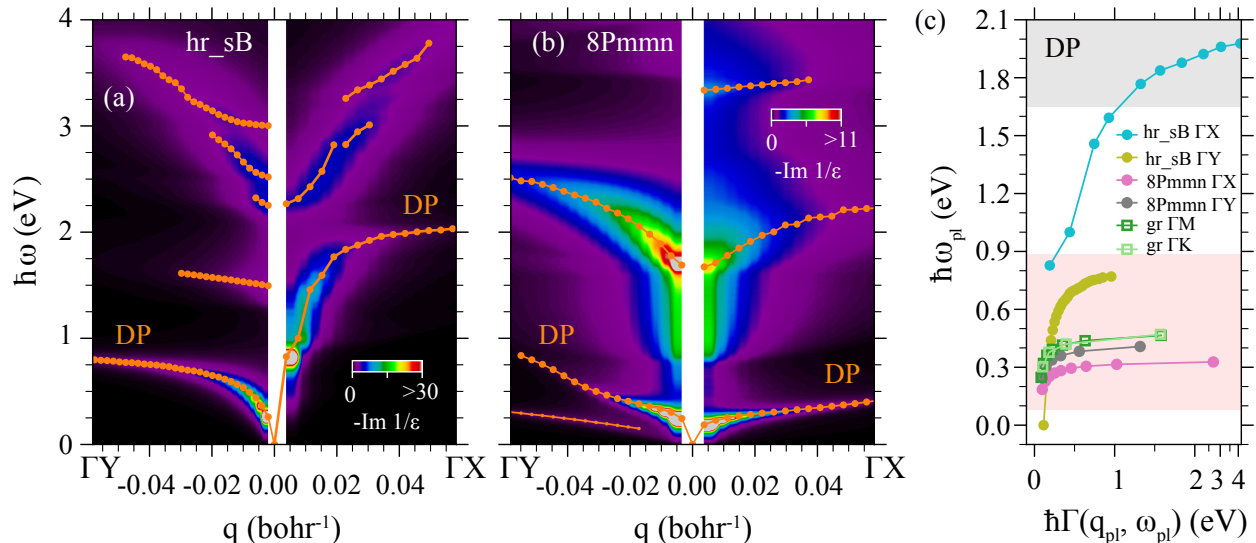


FIG. 7. **Anisotropic electron excitations and damping in borophene.** The electron energy loss function $\text{Im}[1/\varepsilon(\mathbf{q}, \omega)]$ as a function of energy $\hbar\omega$ and momentum q along the ΓX and ΓY directions for (a) the pristine *hr-sB* and (b) the *8Pmmn* ($E_F = -250$ meV) borophene. The orange dots follow the plasmon peaks in these two systems. Both phases show strongly anisotropic Dirac plasmon (DP) mode. (c) The total damping for two phases of borophene and graphene as a function of plasmon frequency $\hbar\omega_{\text{pl}}$ and along the corresponding high symmetry directions. The mid-infrared and visible regions are highlighted with the red and grey shaded areas, respectively.

when temperature rises from $T = 0$ K to $T = 300$ K.

Taking everything into account, these results show a impressive anisotropy in borophene of both plasmon dispersion and plasmon damping along the ΓX and ΓY directions.

In addition, we examine the anisotropic electron excitons in the two phases of borophene in the short-wavelength regime (finite \mathbf{q}). To provide a dispersion relation of the plasmon modes in borophene when $\mathbf{q} > 0$ we calculate the charge-charge response function and the corresponding dielectric function $\varepsilon(\mathbf{q}, \omega)$ [46–48]. The electron energy loss function $\text{Im}[1/\varepsilon(\mathbf{q}, \omega)]$ for two phases of borophene is illustrated in Figs. 7(a) and 7(b) for $q \leq 0.06$ bohr $^{-1}$ and $\omega \leq 4.0$ eV. Note that for the smallest momentum the Dirac plasmon dispersion obtained by the charge-charge (longitudinal) response formalism is in good agreement with the results obtained by means of the current-current (transverse) response theory. For larger momenta, the remarkable anisotropy of Dirac plasmon in borophene is even more pronounced. Especially for the *hr-sB* phase, where plasmons energies, for instance, at $q = 0.06$ bohr $^{-1}$ are $\hbar\omega_{\text{pl}} \approx 2$ eV and $\hbar\omega_{\text{pl}} \approx 0.8$ eV along the ΓX and ΓY directions, respectively. Also, the plasmon energy in the *hr-sB* phase reaches the visible range along the ΓX direction due to intrinsic high carrier density as well as the low intensity of interband transitions (and therefore minor interband screening) for the x polarization [see Fig. 3(c)]. Relevant low intensity interband transitions are here interband continuum (*iii*) at around 1 eV discussed above [see Figs. 4(c) and 4(d)]. On the

other hand, strong interband feature (*ii*) at around 1.5 eV screens and pushes the Dirac plasmon to lower energies for the y polarization. For both phases of borophene, the interband screening makes the Dirac plasmon dispersionless and most importantly flat. This makes the group velocity of plasmon small, which might be important in the context of real-space localization of plasmon wave packets [49]. Apart from the Dirac plasmons, here we can perceive the presence of the anisotropic screened interband excitations (i.e., interband plasmons). Particularly interesting are the interband excitations in the *8Pmmn* phase that fall into the visible range, due to their high intensity and anisotropy. In addition, an acoustic plasmon is present in the *8Pmmn* phase and it comes from the anisotropic Fermi velocity along two principal directions (i.e., anisotropic Dirac cone) [50].

Ultimately, we inspect the total plasmon damping for $\mathbf{q} > 0$, which is shown in Fig. 7(c). It turns out that in the *hr-sB* phase the Dirac plasmon along the ΓX direction is strongly damped for energies in the visible range (i.e., $\hbar\Gamma > 1$ eV). The corresponding plasmon along the ΓY direction, which falls into the mid-infrared region, is, on the other hand, moderately damped. In accordance with our conclusions for the plasmon damping in the long-wavelength limit, the plasmon decay rates of the hole-doped *8Pmmn* borophene and graphene are similar. The unique considerable difference is the anisotropy of plasmon damping for the *8Pmmn* borophene.

CONCLUSION

By using the density functional theory-based calculations we have examined optical properties and collective electron excitation modes (i.e., plasmons) in two phases of single-layer boron (borophene) that host Dirac fermions with tilted Dirac cone, namely the so-called *hr-sB* and *8Pmmn* borophene. According to our numerical results, both of these phases are dynamically stable and are characterized with a strongly anisotropic electronic structure and optical absorption. In fact, hyperbolic plasmonic surfaces appear in the visible range. The *hr-sB* phase, with tilted Dirac cone and nodal line, supports strong hyperbolic Dirac plasmons already in the pristine form owing to the excessive concentration of carriers at the Fermi energy. The *8Pmmn* borophene is a semimetal with Dirac point crossing the Fermi level, and therefore supports plasmon modes only upon carrier doping. For hole-doped *8Pmmn* phase we have determined hyperbolic Dirac plasmons in the mid-infrared region. By analyzing the coupling of Dirac plasmon with phonons and electron-hole pair excitations, we show that the *8Pmmn* phase has a very low plasmonic damping rate.

Both of these phases of borophene outperform typical two-dimensional Dirac material, i.e., graphene, as an optical and plasmonic device, owing to intrinsic metallic character, strong anisotropy, the appearance of hyperbolic plasmonic surfaces, low plasmon losses, and plasmons in the visible range.

METHODS

Computational details.— Our first-principles calculations are based on the density functional theory (DFT) within the QUANTUM ESPRESSO package [51] using Perdew-Zunger functional for exchange-correlation functional. The plane wave energy cutoff was fixed to 50 Ry. The 2D layers are modeled in periodic cells with 20 Å vacuum in the direction normal to the layer to reduce the interaction between periodic images. The convergence criterion for energy is set to 10^{-8} eV and the atomic positions are relaxed until the Hellmann-Feynman forces are less than 10^{-4} eV/Å. The 2D Brillouin zone (BZ) is sampled using $48 \times 24 \times 1$ and $30 \times 40 \times 1$ kpoint meshes for the *hr-sB* and *8Pmmn* phases of borophene, respectively. To accurately determine the electron-phonon coupling (EPC) constants, we employed recently developed Wannier interpolation technique [52], which has been implemented in the EPW code [53]. To do so, the electronic structure, dynamical matrices, and electron-phonon matrix elements obtained from DFT and density functional perturbation theory (DFPT) [54] calculations and they were used as the initial data for Wannier interpolation within the maximally-localized-Wannier-functions formalism.

Optical absorption, phonon-induced damping, and electron excitation spectrum.— In this section,

we present a short theoretical description of optical absorption quantities in the long-wavelength limit ($\mathbf{q} \approx 0$) by making use of the current-current response tensor $\Pi_\mu(\mathbf{q}, \omega)$ calculated within DFT, where the electromagnetic interaction is mediated by the free-photon propagator. The thorough description of the method can be found in our previous works [42, 55, 56].

The optical conductivity can be calculated as $\sigma_\mu(\omega) = -i \lim_{\mathbf{q} \rightarrow 0} \Pi_\mu^0(\mathbf{q}, \omega)/\omega$, while the optical absorption is given by $A(\mathbf{q}, \omega) = -4\hbar \text{Im} \Pi_\mu(\mathbf{q}, \omega)/\omega$ [42, 55, 57], where $\Pi_\mu^0(\mathbf{q}, \omega)$ is a bare current-current tensor, while $\Pi_\mu(\mathbf{q}, \omega)$ is a fully screened tensor.

To investigate the effects of phonons on the plasmon dispersion, we implement the formalism presented in Refs. [57, 58]. Optical excitations are first convenient to decompose into the intraband ($n = m$) and interband ($n \neq m$) contributions, i.e., $\Pi_\mu^0 = \Pi_\mu^{0,\text{intra}} + \Pi_\mu^{0,\text{inter}}$. The electron-phonon scattering mechanism is then considered in the intraband channel.

In the optical limit when $\mathbf{q} \approx 0$, the non-interacting interband current-current response tensor is

$$\begin{aligned} \Pi_\mu^{0,\text{inter}}(\omega) &= \frac{2}{V} \sum_{\mathbf{k}, n \neq m} \frac{\hbar\omega}{E_n(\mathbf{k}) - E_m(\mathbf{k})} \\ &\times |J_{nm\mathbf{k}}^\mu|^2 \frac{f_n(\mathbf{k}) - f_m(\mathbf{k})}{\hbar\omega + i\eta + E_n(\mathbf{k}) - E_m(\mathbf{k})}, \end{aligned} \quad (3)$$

where $J_{nm\mathbf{k}}^\mu$ are the current vertices, $E_n(\mathbf{k})$ are the Kohn-Sham energies, $f_n(\mathbf{k})$ is the Fermi-Dirac distribution function at temperature T , μ are the polarization directions, and V is the normalized volume. Further, the summation over \mathbf{k} wavevectors is carried on a $200 \times 70 \times 1$ ($180 \times 240 \times 1$) grid for *hr-sB* (*8Pmmn*) phase of borophene, n band index sums over 30 electronic bands.

The corresponding intraband contribution of current-current response tensor can be written as the following [57, 59]:

$$\Pi_\mu^{0,\text{intra}}(\omega) = \frac{2}{V} \frac{\omega}{\omega[1 + \lambda_{\text{ph}}(\omega)] + i/\tau_{\text{ph}}(\omega)} \sum_{\mathbf{k}, n} \frac{\partial f_{nk}}{\partial E_{nk}} |J_{nm\mathbf{k}}^\mu|^2. \quad (4)$$

Here the effects of the EPC are contained in the temperature-dependent dynamical scattering time and energy renormalization parameters, i.e., $\tau_{\text{ph}}(\omega)$ and $\lambda_{\text{ph}}(\omega)$, respectively. The dynamical scattering time is given by [60, 61]

$$\begin{aligned} \hbar/\tau_{\text{ph}}(\omega) &= \frac{\pi\hbar}{\omega} \int d\Omega \alpha^2 F(\Omega) \left[2\omega \coth \frac{\Omega}{2k_B T} \right. \\ &\left. - (\omega + \Omega) \coth \frac{\omega + \Omega}{2k_B T} + (\omega - \Omega) \coth \frac{\omega - \Omega}{2k_B T} \right] \end{aligned} \quad (5)$$

where k_B is the Boltzmann constant and $\alpha^2 F(\Omega)$ is the Eliashberg spectral function [57, 58]

$$\alpha^2 F(\omega) = \frac{1}{2\pi N(e_F)} \sum_{\mathbf{q}\nu} \delta(\omega - \omega_{\mathbf{q}\nu}) \frac{\gamma_{\mathbf{q}\nu}}{\hbar\omega_{\mathbf{q}\nu}}, \quad (6)$$

in which $\omega_{\mathbf{q}\nu}$ and $\gamma_{\mathbf{q}\nu}$ are the frequency and linewidth for phonon mode ν at wavevector \mathbf{q} , $N(e_F)$ is the density of states at the Fermi level. Finally, the dynamical energy renormalization parameter $\lambda_{\text{ph}}(\omega)$ is obtained by performing the Kramers-Kronig transformation of $1/\tau_{\text{ph}}(\omega)$.

The total EPC constant can be determined by either Brillouin-zone summation or the frequency-space integration.

$$\lambda = \sum_{\mathbf{q}\nu} \lambda_{\mathbf{q}\nu} = 2 \int \frac{\alpha^2 F(\omega)}{\omega} d\omega, \quad (7)$$

where $\lambda_{\mathbf{q}\nu}$ is the mode- and momentum-resolved EPC constant. Notice that the phonon properties (i.e., phonon energies and electron-phonon matrix elements), needed for calculating $\alpha^2 F(\omega)$ are obtained within the EPW code [53]. The calculations of the EPC constants and Eliashberg function are performed on dense grids of 400×200 (120×160) \mathbf{k} - and 80×40 (30×40) \mathbf{q} -points for *hr-sB* (*8Pmmn*) phase of borophene, which ensures the numerical convergence of the results presented in this work. Having considered these results, we can calculate scattering rate by using Eq. (5) and finally the phonon-induced plasmon decay for both phases of borophene.

The electronic excitation spectra within the random-phase approximation (RPA) for finite momentum ($\mathbf{q} > 0$) are calculated by means of charge-charge correlation function formalism. The dielectric function in the RPA is given by

$$\varepsilon_{\mathbf{G}\mathbf{G}'}(\mathbf{q}, \omega) = \delta_{\mathbf{G}\mathbf{G}'} - \sum_{\mathbf{G}_1} v_{\mathbf{G}\mathbf{G}_1}(\mathbf{q}) \chi_{\mathbf{G}_1\mathbf{G}'}^0(\mathbf{q}, \omega), \quad (8)$$

where the charge-charge correlation function is given by

$$\begin{aligned} \chi_{\mathbf{G}\mathbf{G}'}^0(\mathbf{q}, \omega) &= \frac{2}{V} \sum_{\mathbf{k}, nm} \frac{f_n(\mathbf{k}) - f_m(\mathbf{k} + \mathbf{q})}{\hbar\omega + i\eta + E_n(\mathbf{k}) - E_m(\mathbf{k} + \mathbf{q})} \\ &\times M_{n\mathbf{k}, m\mathbf{k}+\mathbf{q}}(\mathbf{G}) M_{n\mathbf{k}, m\mathbf{k}+\mathbf{q}}^*(\mathbf{G}'). \end{aligned} \quad (9)$$

Here \mathbf{G} is the reciprocal lattice wave vector and $v_{\mathbf{G}\mathbf{G}'}$ is the bare Coulomb interaction. The charge matrix elements are defined as

$$M_{n\mathbf{k}, m\mathbf{k}+\mathbf{q}}(\mathbf{G}) = \left\langle \psi_{n\mathbf{k}} \left| e^{-i(\mathbf{q}+\mathbf{G})\mathbf{r}} \right| \psi_{m\mathbf{k}+\mathbf{q}} \right\rangle_V, \quad (10)$$

where $\psi_{n\mathbf{k}}(\mathbf{r})$ are Kohn-Sham wave functions. The electron energy loss spectrum is obtained by calculating

$$\text{EELS} = -\text{Im} [1/\varepsilon_{\mathbf{G}\mathbf{G}'}(\mathbf{q}, \omega)]_{\mathbf{G}=\mathbf{G}'=0}, \quad (11)$$

which, in addition, contains plasmon poles at $\hbar\omega_{\text{pl}}$ as well as the screened interband and intraband excitations. The corresponding calculations are performed within the GPAW [62] code using the PAW pseudopotentials with energy cutoff of 600 eV, LDA functional, and a $30 \times 20 \times 1$ ($20 \times 30 \times 1$) electron-momentum grid for *hr-sB* (*8Pmmn*). The denser \mathbf{k} grids are used for the summations performed in Eq. (9), namely $300 \times 200 \times 1$ and $200 \times 300 \times 1$ for *hr-sB* and *8Pmmn*, respectively. We include up to 30 electronic bands, $\eta = 30$ meV for the broadening parameter, and the cutoff is 10 eV for the \mathbf{G} vectors. Notice we are convinced that ground state properties (i.e., electronic band structure) obtained from the two separate DFT codes are practically identical.

ACKNOWLEDGMENTS

D.N. acknowledges financial support from the Croatian Science Foundation (Grant no. UIP-2019-04-6869) and from the European Regional Development Fund for the ‘‘Center of Excellence for Advanced Materials and Sensing Devices’’ (Grant No. KK.01.1.1.01.0001). R. A. was supported by the Australian Research Council Centre of Excellence in Future Low-Energy Electronics Technologies (project number CE170100039).

-
- [1] Alexander Poddubny, Ivan Iorsh, Pavel Belov, and Yuri Kivshar, ‘‘Hyperbolic metamaterials,’’ *Nature photonics* **7**, 948 (2013).
 - [2] Jingbo Sun, Natalia M. Litchinitser, and Ji Zhou, ‘‘Indefinite by nature: From ultraviolet to terahertz,’’ *ACS Photonics* **1**, 293 (2014).
 - [3] Morten Niklas Gjerding, Ren e Petersen, Thomas Garn Pedersen, N Asger Mortensen, and Kristian Sommer Thygesen, ‘‘Layered van der waals crystals with hyperbolic light dispersion,’’ *Nature communications* **8**, 1–8 (2017).
 - [4] Souvik Biswas, William S Whitney, Meir Y Grajower, Kenji Watanabe, Takashi Taniguchi, Hans A Bechtel, George R Rossman, and Harry A Atwater, ‘‘Tunable intraband optical conductivity and polarization-dependent epsilon-near-zero behavior in black phosphorus,’’ *Science Advances* **7**, eabd4623 (2021).
 - [5] Mingze He, Sami I Halimi, Thomas G Folland, Sai S Sunku, Song Liu, James H Edgar, Dmitri N Basov, Sharon M Weiss, and Joshua D Caldwell, ‘‘Guided mid-ir and near-ir light within a hybrid hyperbolic-material/silicon waveguide heterostructure,’’ *Advanced Materials* **33**, 2004305 (2021).
 - [6] Wei Ting Chen, Alexander Y Zhu, and Federico Capasso, ‘‘Flat optics with dispersion-engineered metasurfaces,’’ *Nature Reviews Materials* **5**, 604–620 (2020).
 - [7] Joshua D Caldwell, Andrey V Kretinin, Yiguo Chen, Vincenzo Giannini, Michael M Fogler, Yan Francescato, Chase T Ellis, Joseph G Tischler, Colin R Woods, Alexander J Giles, *et al.*, ‘‘Sub-diffractive volume-confined polaritons in the natural hyperbolic material hexagonal boron nitride,’’ *Nature communications* **5**, 1 (2014).
 - [8] J. S. Gomez-Diaz and Andrea Al u, ‘‘Flatland optics with hyperbolic metasurfaces,’’ *ACS Photonics* **3**, 2211 (2016).
 - [9] Weiliang Ma, Pablo Alonso-Gonz alez, Shaojuan Li,

- Alexey Y. Nikitin, Jian Yuan, Javier Martín-Sánchez, Javier Taboada-Gutiérrez, Iban Amenabar, Peining Li, Saül Vélez, Christopher Tollan, Zhigao Dai, Yupeng Zhang, Sharath Sriram, Kourosh Kalantar-Zadeh, Shuit-Tong Lee, Rainer Hillenbrand, and Qiaoliang Bao, “In-plane anisotropic and ultra-low-loss polaritons in a natural van der waals crystal,” *Nature* **562**, 557 (2018).
- [10] Tony Low, Andrey Chaves, Joshua D. Caldwell, Anshuman Kumar, Nicholas X. Fang, Phaedon Avouris, Tony F. Heinz, Francisco Guinea, Luis Martin-Moreno, and Frank Koppens, “Polaritons in layered two-dimensional materials,” *Nature Materials* **16**, 182 (2016).
- [11] D. N. Basov, Ana Asenjo-Garcia, P. James Schuck, Xiaoyang Zhu, and Angel Rubio, “Polariton panorama,” *Nanophotonics* **10**, 549 (2021).
- [12] Chong Wang, Shenyang Huang, Qiaoxia Xing, Yuangang Xie, Chaoyu Song, Fanjie Wang, and Hugen Yan, “Van der waals thin films of wte₂ for natural hyperbolic plasmonic surfaces,” *Nature communications* **11**, 1–9 (2020).
- [13] Chong Wang, Yangye Sun, Shenyang Huang, Qiaoxia Xing, Guowei Zhang, Chaoyu Song, Fanjie Wang, Yuangang Xie, Yuchen Lei, Zhengzong Sun, and Hugen Yan, “Tunable plasmons in large-area wte₂ thin films,” *Phys. Rev. Applied* **15**, 014010 (2021).
- [14] Zahra Torbatian, Dino Novko, and Reza Asgari, “Tunable low-loss hyperbolic plasmon polaritons in a t-d-wte₂ single layer,” *Physical Review Applied* **14**, 044014 (2020).
- [15] D Correias-Serrano, J S Gomez-Diaz, A Alvarez Melcon, and Andrea Alù, “Black phosphorus plasmonics: anisotropic elliptical propagation and nonlocality-induced canalization,” *Journal of Optics* **18**, 104006 (2016).
- [16] Edo van Veen, Andrei Nemilentsau, Anshuman Kumar, Rafael Roldán, Mikhail I. Katsnelson, Tony Low, and Shengjun Yuan, “Tuning two-dimensional hyperbolic plasmons in black phosphorus,” *Phys. Rev. Applied* **12**, 014011 (2019).
- [17] Shan Guan, Shao Ying Huang, Yugui Yao, and Shengyuan A. Yang, “Tunable hyperbolic dispersion and negative refraction in natural electride materials,” *Phys. Rev. B* **95**, 165436 (2017).
- [18] Hongwei Wang and Tony Low, “Hyperbolicity in two-dimensional transition metal ditellurides induced by electronic bands nesting,” *Phys. Rev. B* **102**, 241104 (2020).
- [19] Saeideh Edalati-Boostan, Caterina Cocchi, and Claudia Draxl, “Mote₂ as a natural hyperbolic material across the visible and the ultraviolet region,” *Phys. Rev. Materials* **4**, 085202 (2020).
- [20] Ali Ebrahimian and Reza Asgari, “Natural hyperbolicity in layered hexagonal crystal structures,” *Phys. Rev. B* **103**, 035425 (2021).
- [21] Jianzhou Zhao, Weikang Wu, Jiaojiao Zhu, Yunhao Lu, Bin Xiang, and Shengyuan A Yang, “Highly anisotropic two-dimensional metal in monolayer moolc₂,” *Physical Review B* **102**, 245419 (2020).
- [22] Yuefei Huang, Sharmila N Shirodkar, and Boris I Yakobson, “Two-dimensional boron polymorphs for visible range plasmonics: a first-principles exploration,” *Journal of the American Chemical Society* **139**, 17181–17185 (2017).
- [23] Zhongjian Xie, Xiangying Meng, Xiangnan Li, Weiyuan Liang, Weichun Huang, Keqiang Chen, Jianming Chen, Chenyang Xing, Meng Qiu, Bin Zhang, *et al.*, “Two-dimensional borophene: Properties, fabrication, and promising applications,” *Research* **2020** (2020), 10.34133/2020/2624617.
- [24] Luo Yan, Peng-Fei Liu, Hengtao Li, Yong Tang, Junjie He, Xingyong Huang, Bao-Tian Wang, and Liujiang Zhou, “Theoretical dissection of superconductivity in two-dimensional honeycomb borophene oxide b₂o crystal with a high stability,” *npj Computational Materials* **6**, 1–7 (2020).
- [25] Chuang Hou, Guoan Tai, Zenghui Wu, and Jinqian Hao, “Borophene: Current status, challenges and opportunities,” *ChemPlusChem* **85**, 2186–2196 (2020).
- [26] Sahar Izadi Vishkayi and Meysam Bagheri Tagani, “Current–voltage characteristics of borophene and borophene sheets,” *Physical Chemistry Chemical Physics* **19**, 21461–21466 (2017).
- [27] Miao Gao, Qi-Zhi Li, Xun-Wang Yan, and Jun Wang, “Prediction of phonon-mediated superconductivity in borophene,” *Physical Review B* **95**, 024505 (2017).
- [28] Lyudmyla Adamska, Sridhar Sadasivam, Jonathan J. Foley, Pierre Darancet, and Sahar Sharifzadeh, “First-principles investigation of borophene as a monolayer transparent conductor,” *The Journal of Physical Chemistry C* **122**, 4037 (2018).
- [29] Chao Lian, Shi-Qi Hu, Jin Zhang, Cai Cheng, Zhe Yuan, Shiwu Gao, and Sheng Meng, “Integrated plasmonics: Broadband dirac plasmons in borophene,” *Physical Review Letters* **125**, 116802 (2020).
- [30] Anubhab Haldar, Cristian L Cortes, Pierre Darancet, and Sahar Sharifzadeh, “Microscopic theory of plasmons in substrate-supported borophene,” *Nano Letters* (2020), 10.1021/acs.nanolett.9b04789.
- [31] Sina Abedini Dereshgi, Zizhuo Liu, and Koray Aydin, “Anisotropic localized surface plasmons in borophene,” *Opt. Express* **28**, 16725 (2020).
- [32] Sina Abedini Dereshgi, Zizhuo Liu, and Koray Aydin, “Anisotropic localized surface plasmons in borophene,” *Optics express* **28**, 16725–16739 (2020).
- [33] Andrew J Mannix, Xiang-Feng Zhou, Brian Kiraly, Joshua D Wood, Diego Alducin, Benjamin D Myers, Xiaolong Liu, Brandon L Fisher, Ulises Santiago, Jeffrey R Guest, *et al.*, “Synthesis of borophenes: Anisotropic, two-dimensional boron polymorphs,” *Science* **350**, 1513–1516 (2015).
- [34] Baojie Feng, Jin Zhang, Qing Zhong, Wenbin Li, Shuai Li, Hui Li, Peng Cheng, Sheng Meng, Lan Chen, and Kehui Wu, “Experimental realization of two-dimensional boron sheets,” *Nature chemistry* **8**, 563–568 (2016).
- [35] Alejandro Lopez-Bezanilla and Peter B Littlewood, “Electronic properties of 8- pmmn borophene,” *Physical Review B* **93**, 241405 (2016).
- [36] Sonu Verma, Alestin Mawrie, and Tarun Kanti Ghosh, “Effect of electron-hole asymmetry on optical conductivity in 8- p m m n borophene,” *Physical Review B* **96**, 155418 (2017).
- [37] Krishanu Sadhukhan and Amit Agarwal, “Anisotropic plasmons, friedel oscillations, and screening in 8- p m m n borophene,” *Physical Review B* **96**, 035410 (2017).
- [38] Baojie Feng, Osamu Sugino, Ro-Ya Liu, Jin Zhang, Ryu Yukawa, Mitsuki Kawamura, Takushi Imori, Howon Kim, Yukio Hasegawa, Hui Li, *et al.*, “Dirac fermions in borophene,” *Physical review letters* **118**, 096401 (2017).
- [39] Karim M. Omambac, Marin Petrović, Pantelis Bampoulis, Christian Brand, Marko A. Kriegel, Pascal

- Dreher, David Janoschka, Ulrich Hagemann, Nils Hartmann, Philipp Valerius, Thomas Michely, Frank J. Meyer zu Heringdorf, and Michael Horn-von Hoegen, “Segregation-enhanced epitaxy of borophene on ir(111) by thermal decomposition of borazine,” *ACS Nano* **15**, 7421 (2021).
- [40] Honghong Zhang, Yuee Xie, Zhongwei Zhang, Chengyong Zhong, Yafei Li, Zhongfang Chen, and Yuanping Chen, “Dirac nodal lines and tilted semi-dirac cones coexisting in a striped boron sheet,” *The journal of physical chemistry letters* **8**, 1707–1713 (2017).
- [41] Roland Hayn, Te Wei, Vyacheslav M. Silkin, and Jeroen van den Brink, “Plasmons in anisotropic dirac systems,” *Phys. Rev. Materials* **5**, 024201 (2021).
- [42] Zahra Torbatian and Reza Asgari, “Optical absorption properties of few-layer phosphorene,” *Physical Review B* **98**, 205407 (2018).
- [43] Farnood Ghohroodi Ghamsari and Reza Asgari, “Plasmon-phonon-polaritons in encapsulated phosphorene,” *Plasmonics* **15**, 1289–1304 (2020).
- [44] Dino Novko, “First-principles study of ultrafast dynamics of dirac plasmon in graphene,” *New Journal of Physics* **23**, 043023 (2021).
- [45] Ivan Kupčić, “Damping effects in doped graphene: The relaxation-time approximation,” *Physical Review B* **90**, 205426 (2014).
- [46] Vito Despoja, Dino Novko, Krešimir Dekanić, Marijan Šunjić, and Leonardo Marušić, “Two-dimensional and π plasmon spectra in pristine and doped graphene,” *Physical Review B* **87**, 075447 (2013).
- [47] Zahra Torbatian and Reza Asgari, “Plasmon modes of bilayer molybdenum disulfide: A density functional study,” *Journal of Physics: Condensed Matter* **29**, 465701 (2017).
- [48] Zahra Torbatian and Reza Asgari, “Plasmonic physics of 2d crystalline materials,” *Applied Sciences* **8**, 238 (2018).
- [49] Felipe H. da Jornada, Lede Xian, Angel Rubio, and Steven G. Louie, “Universal slow plasmons and giant field enhancement in atomically thin quasi-two-dimensional metals,” *Nature Commun.* **11**, 1013 (2020).
- [50] M Pizarra, A Sindona, P Riccardi, V M Silkin, and J M Pitarke, “Acoustic plasmons in extrinsic free-standing graphene,” *New Journal of Physics* **16**, 083003 (2014).
- [51] Paolo Giannozzi, Stefano Baroni, Nicola Bonini, Matteo Calandra, Roberto Car, Carlo Cavazzoni, Davide Ceresoli, Guido L Chiarotti, Matteo Cococcioni, Ismaila Dabo, Andrea Dal Corso, Stefano de Gironcoli, Stefano Fabris, Guido Fratesi, Ralph Gebauer, Uwe Gerstmann, Christos Gougoussis, Anton Kokalj, Michele Lazzeri, Layla Martin-Samos, Nicola Marzari, Francesco Mauri, Riccardo Mazzarello, Stefano Paolini, Alfredo Pasquarello, Lorenzo Paulatto, Carlo Sbraccia, Sandro Scandolo, Gabriele Sclauzero, Ari P Seitsonen, Alexander Smogunov, Paolo Umari, and Renata M Wentzcovitch, “Quantum espresso: a modular and open-source software project for quantum simulations of materials,” *Journal of Physics: Condensed Matter* **21**, 395502 (2009).
- [52] Arash A. Mostofi, Jonathan R. Yates, Young-Su Lee, Ivo Souza, David Vanderbilt, and Nicola Marzari, “wannier90: A tool for obtaining maximally-localised wannier functions,” *Computer Physics Communications* **178**, 685 (2008).
- [53] Samuel Poncé, Elena R Margine, Carla Verdi, and Feliciano Giustino, “Epw: Electron–phonon coupling, transport and superconducting properties using maximally localized wannier functions,” *Computer Physics Communications* **209**, 116–133 (2016).
- [54] Stefano Baroni, Stefano de Gironcoli, Andrea Dal Corso, and Paolo Giannozzi, “Phonons and related crystal properties from density-functional perturbation theory,” *Rev. Mod. Phys.* **73**, 515 (2001).
- [55] Dino Novko, Marijan Šunjić, and Vito Despoja, “Optical absorption and conductivity in quasi-two-dimensional crystals from first principles: Application to graphene,” *Physical Review B* **93**, 125413 (2016).
- [56] Zahra Torbatian, Mohammad Alidoosti, Dino Novko, and Reza Asgari, “Low-loss two-dimensional plasmon modes in antimonene,” *Physical Review B* **101**, 205412 (2020).
- [57] Dino Novko, “Dopant-induced plasmon decay in graphene,” *Nano Letters* **17**, 6991 (2017).
- [58] Fabio Caruso, Dino Novko, and Claudia Draxl, “Phonon-assisted damping of plasmons in three- and two-dimensional metals,” *Physical Review B* **97**, 205118 (2018).
- [59] P. B. Allen, “Electron-phonon effects in the infrared properties of metals,” *Phys. Rev. B* **3**, 305–320 (1971).
- [60] Dino Novko, “Broken adiabaticity induced by lifshitz transition in mos 2 and ws 2 single layers,” *Communications Physics* **3**, 1–7 (2020).
- [61] Dino Novko, “Nonadiabatic coupling effects in mgb 2 re-examined,” *Physical Review B* **98**, 041112 (2018).
- [62] J Enkovaara, C Rostgaard, J J Mortensen, J Chen, M Dulak, L Ferrighi, J Gavnholt, C Glinsvad, V Haikola, H A Hansen, H H Kristoffersen, M Kuisma, A H Larsen, L Lehtovaara, M Ljungberg, O Lopez-Acevedo, P G Moses, J Ojanen, T Olsen, V Petzold, N A Romero, J Stausholm-Møller, M Strange, G A Tritsarlis, M Vanin, M Walter, B Hammer, H Häkkinen, G K H Madsen, R M Nieminen, J K Nørskov, M Puska, T T Rantala, J Schiøtz, K S Thygesen, and K W Jacobsen, “Electronic structure calculations with GPAW: a real-space implementation of the projector augmented-wave method,” *Journal of Physics: Condensed Matter* **22**, 253202 (2010).